

# In Situ Generated $\beta$ -Yb<sub>2</sub>Si<sub>2</sub>O<sub>7</sub> Containing Coatings for Steel Protection in Extreme Combustion Environments

Mateus Lenz Leite, Antoine Viard, Dušan Galusek, and Günter Motz\*

The rapid permeation and degradation of silazane-based coatings by water vapor limit their application in combustion environments. Hence, this work reports on the reaction of the oligosilazane Durazane 1800 with an appropriate Yb-complex by a molecular approach and its application as protective thin coatings (1.2  $\mu\text{m}$ ) for AISI 304 in comparison with the benchmark Durazane 2250 in combustion-like environments. Fourier transform infrared- and nuclear magnetic resonance-spectroscopy elucidate the reaction mechanism and the chemical structure of the resulting Yb-modified silazanes, whereas elemental and X-ray diffractometry analyses confirm the formation of crystalline  $\beta$ -Yb<sub>2</sub>Si<sub>2</sub>O<sub>7</sub> and SiO<sub>2</sub> after pyrolysis at 1000 °C in air. Energy dispersive spectroscopy and X-ray photoelectron spectroscopy profile analyses show the enhanced diffusion of Fe, Cr, and Mn from the substrate into the Yb50 coating, which is responsible for a better adhesion (23.7 MPa), scratch tolerance (38 N), and a decreased coefficient of thermal expansion-mismatch to the substrate, resisting 9 thermal cycles between 1000 and 20 °C. Despite the low Yb-silicate content (6.8 wt%), only minor damage is caused to the Yb50 coating after wet oxidation in moist flowing air (1000 °C for 15 h), whereas the Durazane 2250 coating spalled-off. This is a clear indication of the potential of the Yb<sub>2</sub>Si<sub>2</sub>O<sub>7</sub>-containing coatings to protect metals and ceramics in extreme combustion environments.

is additionally restricted by oxidation and corrosion. At such high temperatures, the formation of a chromia passivating layer slows down these adverse effects. However, its rapid degradation due to the depletion of chromium at above 950 °C and the risk of spallation of the protective oxide scale upon thermal cycling reduce their service life. Yearly, the global impact of corrosion is estimated to be US\$ 2.5 trillion, equivalent to 3.4% of the global gross domestic product of 2013. The implementation of corrosion control practices could represent savings between 15% and 35%. In addition, by enabling an extended service life of these alloys at higher temperatures, increased thermal efficiencies and reduced maintenance costs are achievable.<sup>[1–7]</sup>

Within this scope, the deposition of silicon-based coatings is an efficient approach to increase the oxidation and corrosion resistance of alloys at high temperatures, which are commonly deposited by intricate methods as chemical and physical vapor deposition.<sup>[8–16]</sup> In contrast, the polymer derived ceramics

(PDC) route enables the application of silicon-based precursors (e.g., silazanes, siloxanes, and carbosilanes) as coatings by simple polymer processing methods such as dip-,<sup>[11–13]</sup> spray-,<sup>[16,17]</sup> or spin-coating.<sup>[18]</sup> These coatings are thermally treated to induce their cross-linking into thermosets, followed by their conversion into amorphous ceramics at temperatures above 400 °C.<sup>[15,19,20]</sup> Among the suitable precursors for the processing of coatings, silazanes stand out because of their commercial availability, high ceramic yield, and strong adhesion to most substrates. Their outstanding oxidation and corrosion performance rely on the formation of a slow growing SiO<sub>2</sub>-scale, known for the lowest oxygen permeability among the simple oxides.<sup>[21]</sup> The main drawback of the PDCs is related to the polymer to ceramic transition, which is accompanied by an increase in density and leading to a volume shrinkage exceeding 50%.<sup>[19,22]</sup> Therefore, the critical thickness of unfilled coatings is less than 3.5  $\mu\text{m}$ .<sup>[11,12,23]</sup> Nevertheless, only 1  $\mu\text{m}$  thin Durazane 2250 (perhydropolysilazane) coatings are already capable of protecting stainless steel substrates against oxidation up to 10 h at 1000 °C in air.<sup>[12]</sup>

However, H<sub>2</sub>O<sub>(v)</sub> and CO<sub>2</sub> are main products of combustion and may also act as primary oxidants. In such environments, the faster permeation of water vapor through Si-based films when compared to molecular oxygen is capable of intensifying

## 1. Introduction

Chromia forming alloys (e.g., stainless steels and nickel-based superalloys) are widely used as structural materials for aircrafts, industry, and military. More specifically in extreme combustion environments (e.g., gas turbines and exhaust lines), where the service temperature can exceed 1000 °C, their application

M. Lenz Leite, Dr. A. Viard, Dr. G. Motz  
Department of Ceramic Materials Engineering  
University of Bayreuth  
Prof.-R.-Bormann-Str. 1, 95447 Bayreuth, Germany  
E-mail: guenter.motz@uni-bayreuth.de

Prof. D. Galusek  
Centre for Functional and Surface Functionalised Glass (FunGlass)  
Alexander Dubček University of Trenčín  
Študentská 2, Trenčín 911 50, Slovakia

 The ORCID identification number(s) for the author(s) of this article can be found under <https://doi.org/10.1002/admi.202100384>.

© 2021 The Authors. Advanced Materials Interfaces published by Wiley-VCH GmbH. This is an open access article under the terms of the Creative Commons Attribution License, which permits use, distribution and reproduction in any medium, provided the original work is properly cited.

DOI: 10.1002/admi.202100384

the effects related to oxidation of chromia forming alloys.<sup>[1,7,24,25]</sup> Moreover, the rapid degradation of silazane-based coatings by hot gas corrosion at temperatures above 1200 °C due to the formation of volatile Si(OH)<sub>4</sub> represents an upper limit for their application.<sup>[21,24,26,27]</sup>

It has already been proven that the SiO<sub>2</sub>-activity in rare-earth silicates is strongly reduced upon exposure in water vapor containing environments up to 1400 °C.<sup>[17,28–31]</sup> Especially ytterbium silicates are well suited in these extreme conditions due to their enhanced stability and reduced number of polymorphs.<sup>[32,33]</sup> Thus, a suitable approach to increase the stability of silazanes in extreme combustion environments should be the addition of selected elements from the lanthanides series.

The chemical reactions of different metal compounds based on Cu, Fe, Pd, Ti, and Hf with silazanes were comprehensively described. The use of suitable metal complexes ensures a very homogeneous distribution of these elements on an atomic level in the resulting metal modified polymer and subsequently in the ceramic after pyrolysis. Depending on the metal, the precursor ratio, pyrolysis temperature, and atmosphere, the formation of the respective metals or their oxides, carbides, silicides, nitrides, and silicates was reported.<sup>[34–42]</sup>

Therefore, our goal was to increase the stability of silazane-based coatings against hot gas corrosion in combustion environments by modifying the oligosilazane Durazane 1800 with ytterbium in order to yield ytterbium silicates upon pyrolysis in air. In this work, the reaction mechanism between a new Yb-complex (Yb(Ap<sup>TMS</sup>)<sub>3</sub>) with polysilazanes is explored in details as well as their conversion to ceramics. Thereafter, Yb-modified polysilazane coatings were applied onto AISI 304 and compared to the benchmark silazane Durazane 2250. The best resulting coatings were tested against oxidation in dry and wet atmospheres up to 1000 °C, simulating combustion environments. Although the discussion of the results is limited to 1000 °C, the obtained Yb<sub>2</sub>Si<sub>2</sub>O<sub>7</sub> phase should increase the stability of silazane-based ceramic coatings against hot gas corrosion, thus enabling their use at temperatures above 1200 °C.

## 2. Results and Discussion

### 2.1. Synthesis and Characterization of the Ytterbium-Modified Polysilazanes

In previous publications from our group and Kempe et al. the modification of polysilazanes using suitable metal complexes with aminopyridinato ligands was investigated.<sup>[36,37,39,40]</sup> The same strategy was used in the present work considering ytterbium. Various samples with different contents of Yb were synthesized. Elemental analysis was performed with the sample Yb50 to confirm the reaction and the targeted Si to Yb ratio (Table 1). The determined chemical composition (SiC<sub>2.13</sub>N<sub>1.26</sub>Yb<sub>0.02</sub>O<sub>0.05</sub>) is close to the theoretical values (SiC<sub>1.4</sub>N<sub>1.1</sub>Yb<sub>0.02</sub>). The very low oxygen content indicates that the synthesis was well performed under inert conditions. The Si to Yb ratio in the final sample is in accordance with the targeted value fixed for the synthesis, whereas the higher amounts of carbon and nitrogen are attributed to the presence of residual aminopyridinato ligands (Ap<sup>TMS</sup>H) ligands.

**Table 1.** Elemental analysis of Durazane 1800 and Yb50 before and after pyrolysis at 1000 °C in air.

Sample	Composition [mol%]					Empirical formula
	Si	C	N	O	Yb	
Durazane 1800 <sup>[46]</sup>	28.57	40.00	31.43	–	–	Si C <sub>1.4</sub> N <sub>1.1</sub>
Durazane 1800 (1000 °C, air) <sup>[20]</sup>	30.86	35.93	22.10	11.11	–	Si C <sub>1.16</sub> N <sub>0.72</sub> O <sub>0.36</sub>
Yb50*	22.46	47.82	28.19	1.17	0.36	Si C <sub>2.13</sub> N <sub>1.26</sub> O <sub>0.05</sub> Yb <sub>0.02</sub>
Yb50* (theoretical)	25.60	46.86	27.06	0	0.48	Si C <sub>1.4</sub> N <sub>1.1</sub> Yb <sub>0.02</sub>
Yb50 (1000 °C, air)	32.99	2.34	0.55	63.57	0.55	Si C <sub>0.07</sub> N <sub>0.02</sub> O <sub>1.93</sub> Yb <sub>0.02</sub>

\*—Polymer state

In order to investigate the influence of the modification with different amounts of Yb on the chemical structure of Durazane 1800, the Fourier transform infrared (FTIR) spectra of the different synthesized precursors (Yb100 to Yb10) were recorded (Figure 1).

Several bands arising from the chemical groups of Durazane 1800 are noticed in all samples: stretching vibrations of N–H bonds at 3379 cm<sup>-1</sup>, stretching of C–H bonds at 3044, 2956, and 2894 cm<sup>-1</sup>, stretching of Si–H bonds at 2127 cm<sup>-1</sup>, deformation of C–H bonds in SiCH<sub>3</sub> at 1253 cm<sup>-1</sup>, and stretching of Si–N bonds at 891 cm<sup>-1</sup>. The absorption band at 3044 cm<sup>-1</sup> is attributed to the vibration of C–H bonds in vinyl groups and remains unchanged in all spectra showing that these groups are not involved in the reaction. While increasing the amount of Yb incorporated into the polymer, absorption bands arising from the ligands become predominant (1600–500 cm<sup>-1</sup> in the spectra). This is due to the increasing amount of the released Ap<sup>TMS</sup>H ligands from Yb100 to Yb10 during synthesis (Figure 20, Experimental Section), which were not removed from the mixture.

Figure 1 also shows that the absorption band of Si–H bonds remains unchanged, even at high Yb contents (Yb10). An explanation would be that the fixation of Yb preferentially involves

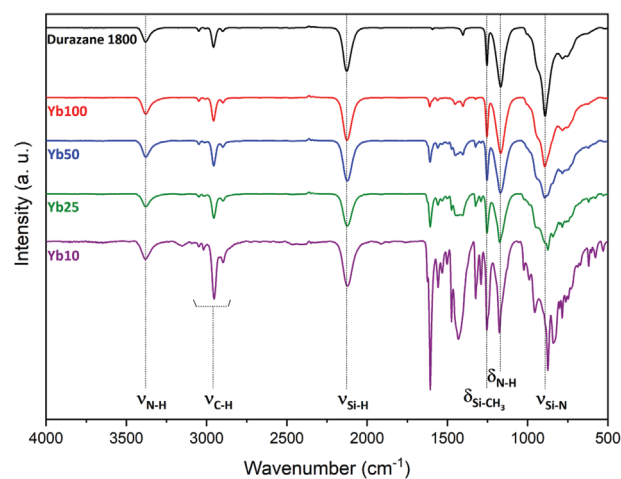


**Figure 1.** FTIR spectra of Durazane 1800, and different Yb-modified polysilazanes (Yb100, Yb50, Yb25, and Yb10).

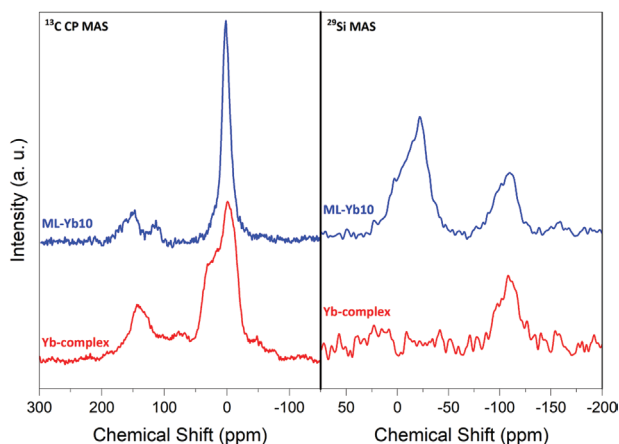


**Figure 2.** Solid state  $^{13}\text{C}$  CP MAS NMR and  $^{29}\text{Si}$  MAS NMR spectra of the Yb-complex and of the Yb-modified Durazane 1033 ML-Yb10.

NH groups, in agreement with the work of Glatz et al.<sup>[37]</sup> Nevertheless, the absorption band related to these groups seems to remain unchanged after reaction, since the release of  $\text{Ap}^{\text{TMS}}\text{H}$  leads to the formation of new NH bonds, thus influencing the detected intensity. FTIR analysis of ML-Yb10 (see Section 4.3) did not provide substantial information concerning the reaction mechanism. However, the absorption bands arising from the ligands were still available, indicating a partial reaction of the ytterbium complex with the silazane during synthesis. To confirm these results, solid state nuclear magnetic resonance (NMR) analyses were performed with this sample (Figure 2).

The  $^{13}\text{C}$  CP MAS NMR spectrum of the Yb-complex ( $\text{Yb}(\text{Ap}^{\text{TMS}})_3$ ) exhibits a major signal at  $-0.9$  ppm arising from  $\text{Si}(\text{CH}_3)$  and a signal around 20 ppm attributed to  $-\text{CH}_3$  groups. Moreover, signals around 130 ppm confirm the presence of aromatic carbon atoms, which is in accordance with the theoretical chemical formula. The  $^{29}\text{Si}$  MAS NMR measurement detected a single signal at  $-107$  ppm, which can only arise from the  $\text{SiC}_3\text{N}$  unit present in the ligand. The  $^{13}\text{C}$  CP MAS NMR spectrum recorded for ML-Yb10 shows a predominant signal at  $-2.2$  ppm associated to  $-\text{CH}_3$  groups, but also signals that arise from aromatic carbons. The  $^{29}\text{Si}$  MAS NMR spectrum exhibits a very broad signal between 10 ppm and  $-30$  ppm, which can be associated to the presence of different units of the type  $\text{SiC}_x\text{N}_y\text{H}_z$  ( $x + y + z = 4$ ).<sup>[43–45]</sup> The broadness of the signal can be linked to the amorphous character and the higher molecular weight of the polymer. A similar signal as detected for the Yb-complex is also present at  $-109$  ppm, which confirms that not all ligands are participating in the reaction. A reason for this could be the steric hindrance of further reactions after the substitution of the first ligand. Since no other signal was detected by the  $^{29}\text{Si}$  MAS NMR, it can be assumed that no ytterbium is present in the near chemical environment of silicon. Such chemical configuration could lead to peaks at lower frequencies, however no example was found in the literature. The NMR results are in good accordance with the previous IR measurements.

Thermogravimetric analyses (TGA) of the of the resulting modified precursors from Table 5 (Experimental Section) confirms that the reaction of the Yb-complex with Durazane 1800 affects its pyrolysis behavior and the final ceramic yield up to  $1000^\circ\text{C}$  in air (Figure 3).

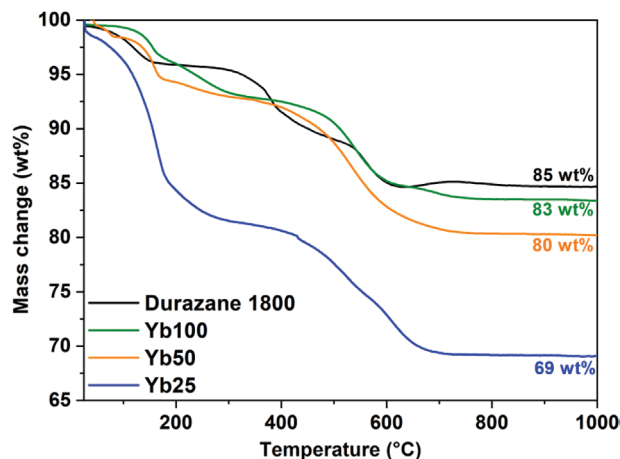


**Figure 3.** Thermogravimetric analyses of Durazane 1800 and the Yb-modified polysilazanes in air up to  $1000^\circ\text{C}$  and heating rate of  $5\text{ K min}^{-1}$  (all samples contained 3 wt% DCP).

The typical polymer to ceramic conversion of Durazane 1800 is characterized by the release of volatile oligomers, ammonia, hydrogen, and methane up to  $750^\circ\text{C}$ . The incorporation of oxygen occurs by the substitution of the  $\text{Si}-\text{N}$  and  $\text{Si}-\text{H}$  bonds of the oligosilazane to form  $\text{Si}-\text{O}-\text{Si}$  bridges during pyrolysis in air, thus increasing its degree of cross-linking. The higher degree of cross-linking hinders the evolution of volatile low molecular weight oligomers during pyrolysis, increasing the ceramic yield, and influencing the final ceramic composition. Motz et al. report the formation of an amorphous ceramic with the elemental composition of  $\text{SiC}_{1.16}\text{N}_{0.72}\text{O}_{0.36}$  and 82 wt% yield at  $1000^\circ\text{C}$ ,<sup>[20]</sup> in good agreement with our measurement. Still from Figure 3, an increased mass loss is detected with increasing Yb content. This change is mainly due to the first stage of the ceramic conversion at temperatures below  $200^\circ\text{C}$ . In regard to Durazane 1800, the lowest Yb-content (Yb100) has only little influence on the pyrolysis behavior and the ceramic yield, whereas the mass loss is significantly increased for Yb50 (20 wt%) and Yb25 (31 wt%). FTIR analysis of Yb10 exposed to air at  $110^\circ\text{C}$  and different times (Figure 4) supports that this result is due to the release of the aminopyridinato ligands.

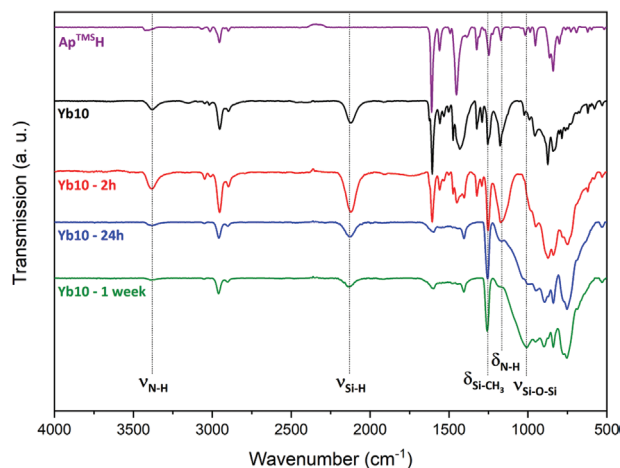


**Figure 4.** FTIR spectra of  $\text{Ap}^{\text{TMS}}\text{H}$  and Yb10 after annealing at  $110^\circ\text{C}$  in air and different times.

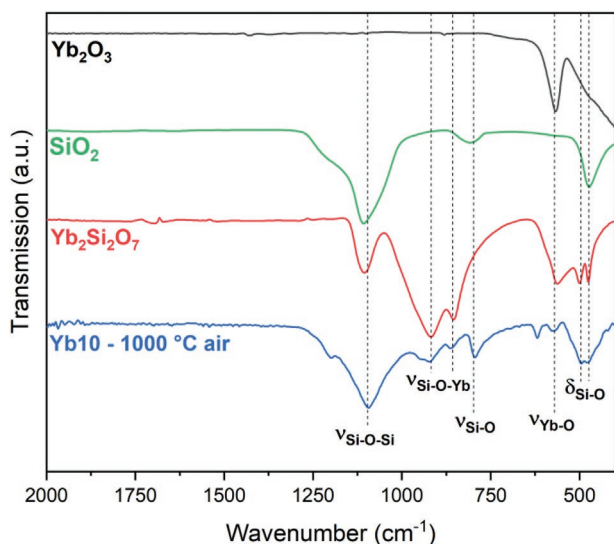


**Figure 5.** FTIR spectrum of Yb10 pyrolyzed at 1000 °C in air in comparison with Yb<sub>2</sub>O<sub>3</sub>, SiO<sub>2</sub>, and Yb<sub>2</sub>Si<sub>2</sub>O<sub>7</sub>.

As the exposure time of Yb10 at 110 °C in air increases, the bands arising from Ap<sup>TM</sup>SH (especially at 1600–1100 cm<sup>-1</sup>) decrease in intensity, indicating its elimination. At the same time, the intensity of the asymmetric Si–O–Si band (approximately 1016 cm<sup>-1</sup>) increases upon the substitution of the N–H and Si–H bonds,<sup>[20]</sup> respectively at 3379, 1165, and 2127 cm<sup>-1</sup>, thereby increasing the degree of cross-linking of the Yb-modified precursors at already low temperatures. The elemental composition of the Yb50 ceramic in Table 1 confirms the remarkable influence of the modification of Durazane 1800 with Yb on its pyrolysis behavior in air.

The pyrolysis of Durazane 1800 in air induces the incorporation of oxygen in the material and leads to the formation of a SiCNO ceramic. Both C and N contents are reduced in the ceramic due to the release of oxidation products during the polymer to ceramic conversion. Nevertheless, the reaction of Durazane 1800 with oxygen leads to the formation of a passivating SiO<sub>2</sub>-scale, which prevents the complete elimination of C and N.<sup>[20]</sup>

In contrast, the chemical composition of Yb50 after pyrolysis at 1000 °C in air demonstrates that C and N were nearly completely substituted by oxygen, whereas the Si to Yb ratio remained stable. Hence, a ceramic with the composition of SiC<sub>0.07</sub>N<sub>0.02</sub>O<sub>1.93</sub>Yb<sub>0.02</sub> was obtained, resembling elemental composition of SiO<sub>2</sub>. Based on these results, it is clear that Yb promotes the significantly faster incorporation of oxygen, which is crucial for self-curing in air and the formation of Yb-silicates. FTIR spectrum of Yb10 after pyrolysis at 1000 °C in air provides additional information about the pyrolysis behavior of the Yb-modified precursors (Figure 5).

No absorption bands between 1500 and 3500 cm<sup>-1</sup> indicate that all organic groups in the starting precursors disappeared during pyrolysis in air, which is confirmed by the elemental analysis of Yb50 (Table 1). In addition, the IR spectrum of Yb10 after pyrolysis is clearly a combination of those resulting from Yb<sub>2</sub>O<sub>3</sub>, SiO<sub>2</sub>, and Yb<sub>2</sub>Si<sub>2</sub>O<sub>7</sub>. The bands at 1094 and 795 cm<sup>-1</sup> correspond to stretching vibrations of asymmetric and symmetric

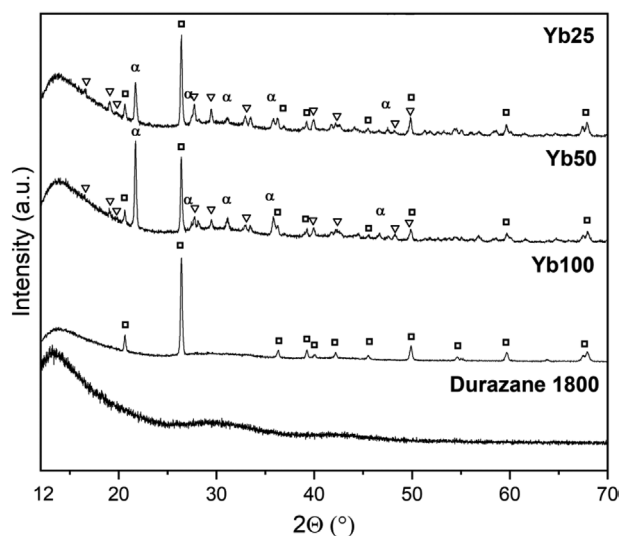


**Figure 6.** XRD diffractograms of the resulting ceramics from Durazane 1800 and the Yb-modified polysilazanes after pyrolysis at 1000 °C in air (□ – SiO<sub>2</sub> (α-Quartz, 04-008-4821); α – SiO<sub>2</sub> (α-Cristobalite, 04-007-2134); ▽ – β-Yb<sub>2</sub>Si<sub>2</sub>O<sub>7</sub> (Keivite, 04-015-6658)).

Si–O bonds, respectively, which are also present in the IR spectra of SiO<sub>2</sub> and Yb<sub>2</sub>Si<sub>2</sub>O<sub>7</sub>. In silanolates, the range between 1000–900 cm<sup>-1</sup> is attributed to Si–O–Metal stretching bonds.<sup>[47]</sup> Hence, in regard to the IR spectrum of Yb<sub>2</sub>Si<sub>2</sub>O<sub>7</sub>, the bands at 919 and 864 cm<sup>-1</sup> from Yb10 were attributed to Si–O–Yb stretching bonds. Carrión et al. and Díaz et al. report that the lower frequency modes in the IR spectrum of rare earth silicates such as Y<sub>2</sub>Si<sub>2</sub>O<sub>7</sub> are rather difficult to be characterized since Si–O and Y–O coexist in similar ranges. In this case, the modes from 600 to 500 cm<sup>-1</sup> are attributed to Y–O stretching, whereas those from 500 to 400 cm<sup>-1</sup> correspond to Si–O bending.<sup>[32,48]</sup> Based on this statement and on the IR spectra of Yb<sub>2</sub>O<sub>3</sub>, SiO<sub>2</sub>, and Yb<sub>2</sub>Si<sub>2</sub>O<sub>7</sub> the bands at 494 and 478 cm<sup>-1</sup> were attributed to Si–O bending, whereas Yb–O stretching bonds were assigned to 572 cm<sup>-1</sup>, indicating the formation of ytterbium silicates besides silica, as confirmed by X-ray diffractometry (XRD) measurements (Figure 6).

Whereas the pyrolysis of Durazane 1800 at 1000 °C in air yields an amorphous ceramic, the lowest concentration of Yb (Yb100) already promoted the crystallization of α-quartz, which was assumed by FTIR (Figure 5) and elemental analyses (Table 1) due to the formation of highly ordered SiO<sub>2</sub> structures. Salmang and Scholze mentioned that the presence of impurities can enhance the crystallization kinetics of a ceramic by acting as nuclei,<sup>[49]</sup> attributed to traces of C and N present in the modified precursors after pyrolysis (Table 1).

By the introduction of small amounts of impurity in the crystal lattice of pure quartz, the transition to cristobalite, which is commonly reported at 1250 °C, can be reduced to 1000 °C,<sup>[49]</sup> as also determined for Yb50 and Yb25.

In addition to crystalline SiO<sub>2</sub> (α-quartz and α-cristobalite), β-Yb<sub>2</sub>Si<sub>2</sub>O<sub>7</sub> (Keivite) crystallized during the pyrolysis of Yb50 and Yb25 in air, arising from the solid-state reaction between Yb<sub>2</sub>O<sub>3</sub> and SiO<sub>2</sub>.<sup>[17]</sup> In this work, the excessive amount of SiO<sub>2</sub> may have favored the formation of the disilicate (Yb<sub>2</sub>Si<sub>2</sub>O<sub>7</sub>)

**Table 2.** Refined lattice parameters and phase quantification of the diffractograms from Figure 6.

Sample	Rwp	GOF	Degree of crystallinity [wt%]	Crystalline phases*	Relative amount [wt%]	Lattice parameters			
						a [Å]	b [Å]	c [Å]	β [°]
Yb100	7.75	1.38	13	SiO <sub>2</sub> (Q)	100	4.919		5.407	
Yb50	7.58	1.34	18	SiO <sub>2</sub> (Q)	40	4.919		5.405	
				SiO <sub>2</sub> (C)	46	4.981		6.956	
				Yb <sub>2</sub> Si <sub>2</sub> O <sub>7</sub> (K)	14	6.792	8.856	4.701	102.12
Yb25	7.92	1.39	20	SiO <sub>2</sub> (Q)	54	4.922		5.409	
				SiO <sub>2</sub> (C)	25	4.985		6.955	
				Yb <sub>2</sub> Si <sub>2</sub> O <sub>7</sub> (K)	21	6.796	8.865	4.704	102.12

\* (Q)— $\alpha$ -Quartz (space group: P3<sub>1</sub>21); (C)— $\alpha$ -Cristobalite (space group: P4<sub>1</sub>2<sub>1</sub>2); (K)—Keivite (space group: C12/m1)

rather than the oxy-monosilicate (Yb<sub>2</sub>SiO<sub>5</sub>), although no clear evidences of the reaction mechanism are available.

Rietveld refinement of the corresponding diffractograms (Figure 6) provides additional information on the crystallization behavior of the pyrolyzed Yb-modified precursors. **Table 2** summarizes the crystalline phase quantification and their respective refined lattice parameters, which are in good agreement with the literature.<sup>[32,49]</sup> Moreover, the low weighted residual (Rwp) values (<10) and the goodness of fit (GOF) index lower than 1.4 indicate the reliability of the refined data.

By increasing the Yb concentration from Yb100 to Yb50, the degree of crystallinity of the resulting ceramics increased from 13 to 18 wt%, achieving a maximum of 20 wt% for Yb25. The reason for the similarity between Yb50 and Yb25 could rely on the elemental composition of the corresponding ceramics. Due to the nearly complete removal of carbon and nitrogen from Yb50 (see Table 1), no great influence on the crystalline degree of the resulting ceramics is expected beyond this concentration. On the one hand, higher concentrations of Yb (Yb25) showed rather a negative effect on the purity of  $\alpha$ -quartz as the relative amount of  $\alpha$ -cristobalite dropped from 46 to 25 wt%, respectively for Yb50 and Yb25. On the other hand, Rietveld refinement confirmed the crystallization of higher amounts of  $\beta$ -Yb<sub>2</sub>Si<sub>2</sub>O<sub>7</sub>, corresponding to 21 wt% of the crystalline phases of Yb25, whereas only 14 wt% was detected for Yb50.

**Table 3** provides an estimation of the theoretical concentration of Yb<sub>2</sub>Si<sub>2</sub>O<sub>7</sub> and the total amount of SiO<sub>2</sub> in the Yb-modified precursors after pyrolysis in air. Therefore, the quantitative oxidation of the Yb-complex and Durazane 1800 into respectively Yb<sub>2</sub>O<sub>3</sub> and SiO<sub>2</sub> was considered, as well as their stoichiometric reaction to yield Yb<sub>2</sub>Si<sub>2</sub>O<sub>7</sub>. As reference, a

**Table 3.** Estimation of the concentration of Yb<sub>2</sub>Si<sub>2</sub>O<sub>7</sub> and SiO<sub>2</sub> in the Yb-modified precursors after pyrolysis in air (in wt%).

Sample	Yb <sub>2</sub> Si <sub>2</sub> O <sub>7</sub>	SiO <sub>2</sub>
Yb100	4.1	95.9
Yb50	8.0	92.0
Yb50*	6.8	93.2
Yb25	15.1	84.9

\*—Based on the elemental composition of Yb50 (1000 °C, air) in Table 1.

comparative to Yb50 (1000 °C, air) based on its elemental composition is provided (see Table 1).

Based on the experimental data of Yb50 (1000 °C, air), only a small difference to the theoretical concentration of Yb<sub>2</sub>Si<sub>2</sub>O<sub>7</sub> and SiO<sub>2</sub> is calculated. This result indicates the elimination of small amounts of Yb during pyrolysis in air, thus leading to a 1.2 wt% lower Yb<sub>2</sub>Si<sub>2</sub>O<sub>7</sub> content. Based on its elemental composition (SiC<sub>0.07</sub>N<sub>0.02</sub>O<sub>1.93</sub>Yb<sub>0.02</sub>), degree of crystallinity and phase composition detected by XRD, a conversion of approximately 37 mol% of atomic Yb into crystalline  $\beta$ -Yb<sub>2</sub>Si<sub>2</sub>O<sub>7</sub> is calculated, which corresponds to 2.52 wt% of the Yb50 ceramic. The rest remains amorphous or not detectable by XRD analysis. Hence, by analyzing Table 3, it is evident that despite the similar degree of crystallinity and crystalline phase composition of Yb50 and Yb25 (Table 2), nearly twice as much Yb<sub>2</sub>Si<sub>2</sub>O<sub>7</sub> should be expected in the Yb25 ceramic. In this case, annealing at higher temperatures and holding times could favor the crystallization of the disilicate phase beyond the detected amount.<sup>[49]</sup>

## 2.2. Characterization of the Coatings

First, the applied coating systems (see Section 4.4) were optically evaluated regarding crack formation or spallation after pyrolysis at 1000 °C in air (**Figure 7**).

From Figure 7, defects are clearly visible at the surface of the Durazane 1800 coated substrate. The dark spots on the coated region represent unprotected areas where the substrate was oxidized during pyrolysis. An improved oxidation protection was already achieved by using the HTTS polysilazane, which was synthesized by the selective cross-linking of Durazane 1800.<sup>[50]</sup> In comparison with Durazane 1800, the increased degree of cross-linking of HTTS prevents the volatilization of oligomers during pyrolysis, which results in higher ceramic yields, leading to the deposition of thicker coatings and avoiding the formation of defects, because of the reduced shrinkage of the polysilazane.<sup>[50]</sup>

Due to the high reactivity of the Yb-modified polysilazanes with oxygen and the resulting increased degree of cross-linking at already low temperatures, a low Yb content as for Yb100 already leads to a similar oxidation protection as for HTTS coatings. Anyway, uniformly distributed defects are visible at its surface, comparable to the Yb25 coated sample. In the latter case, the formation of such defects can be related to the

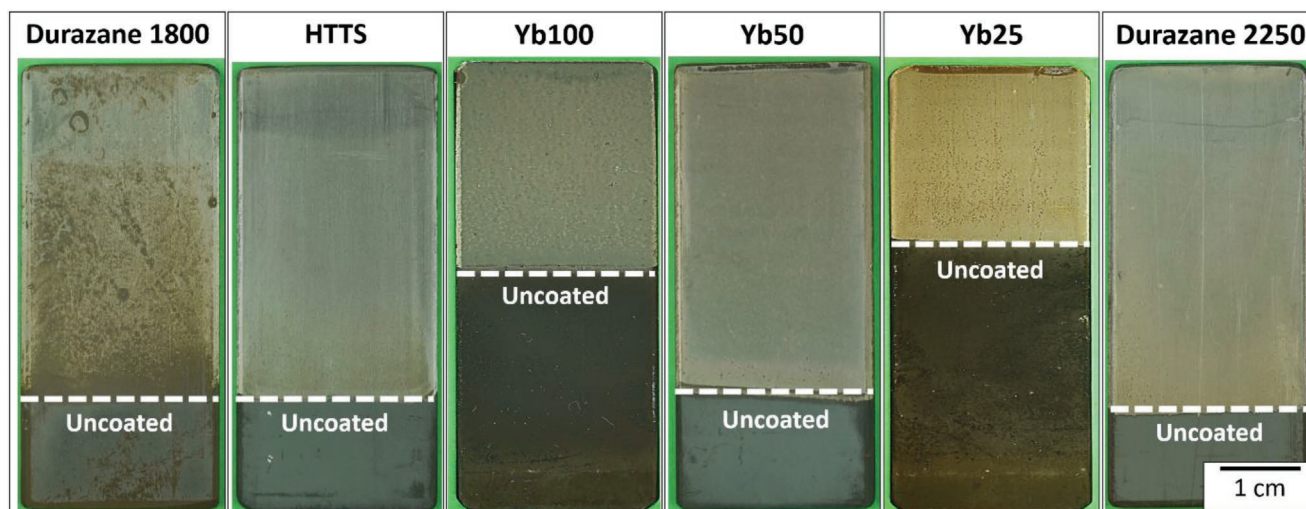


**Figure 7.** Comparison between Durazane 1800 + 3 wt% DCP, HTTS, Yb-modified polysilazanes, and Durazane 2250-based coatings on AISI 304 after pyrolysis at 1000 °C, 1 h in air.

increased mass loss during pyrolysis (refer to Figure 3), caused by the volatilization of the aminopyridinato ligands, whereas the insufficient coating thickness causes the defects at the surface of the Yb100 coated steel sample. In contrast, the Yb50 coating appears defect free, comparable with the HTTS and Durazane 2250 coatings.

As extended oxidation tests at 1000 °C for 10 h in air revealed an insufficient protection of the AISI 304 substrate coated with HTTS, the following discussion focused on the detailed characterization of the Yb50 based coatings and Durazane 2250 coated systems as a benchmark.

In agreement with Günthner et al., the microstructure of the Durazane 2250 coating after pyrolysis (Figure 8a) is characterized by smooth intact areas (region 1) enclosed by a few small cracks from which metal oxides grow (region 2), resulting from the oxidation of the AISI 304 steel,<sup>[12]</sup> as evidenced by scanning electron microscopy (SEM).

Energy dispersive spectroscopy (EDS) point analysis of region 1 confirms the presence of mainly Si and O, respectively 36 and 54 at%, due to the formation of a dense SiO<sub>2</sub>-layer upon pyrolysis in air, slowing the further oxidation of the SiO<sub>x</sub>(N) coating.<sup>[11,12]</sup> Anyhow, 6 at% of Fe and 4 at% of Cr are also present within this region, whereas only traces of Mn were

detected, indicating the diffusion of transition metals from the substrate into the coating. In contrast, EDS analysis of region 2 detected high Mn (54 at%) and O (38 at%) contents, whereas Si, Cr, and Fe corresponded respectively to less than 4 at%. Günthner et al. reported that the cracks (region 2) result from the shrinkage of the coating of up to 48 vol% during pyrolysis. In combination with the high coefficient of thermal expansion (CTE) of AISI 304, the cracking of the coating leads to the oxidation of the substrate and to the formation of a protective Cr<sub>2</sub>O<sub>3</sub>-scale.<sup>[2,11,51]</sup> In our case, the high concentrations of Mn can be explained by its diffusion through the protective Cr<sub>2</sub>O<sub>3</sub>-scale. Due to the exposure of the coated systems at high temperatures, Mn is capable of diffusing through Cr<sub>2</sub>O<sub>3</sub> at faster rates than Fe to form MnCr<sub>2</sub>O<sub>4</sub> or Mn<sub>3</sub>O<sub>4</sub>, resembling the detected composition.<sup>[52]</sup> However, the detection of such phases by means of X-ray diffractometry is rather difficult due to the limited coating thickness.

The back-scattered electron (BSE) analysis of the cross-section of the Durazane 2250 coating reveals a well-adhered and dense layer with a thickness of approximately 1.2 μm (Figure 8b), where region 2 is marked accordingly to Figure 8a. To get more detailed information about the chemical composition of the coatings after pyrolysis at 1000 °C for 1 h in air, X-ray

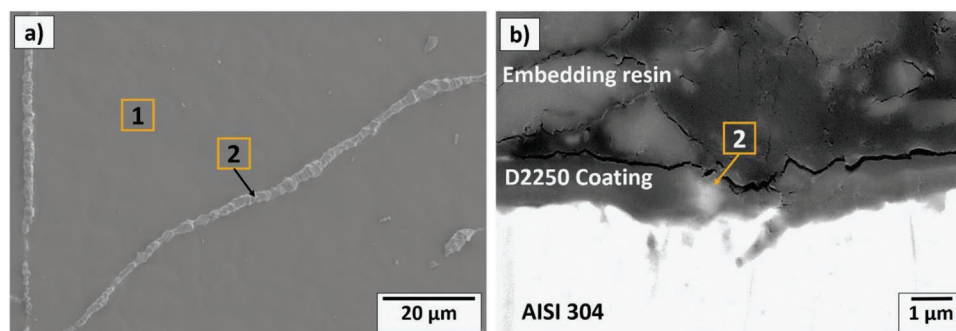


**Figure 8.** SEM/BSE analysis of the a) surface and b) cross-section of the Durazane 2250 (D2250) coating on AISI 304 after pyrolysis at 1000 °C for 1 h in air, and selected points for EDS analysis.

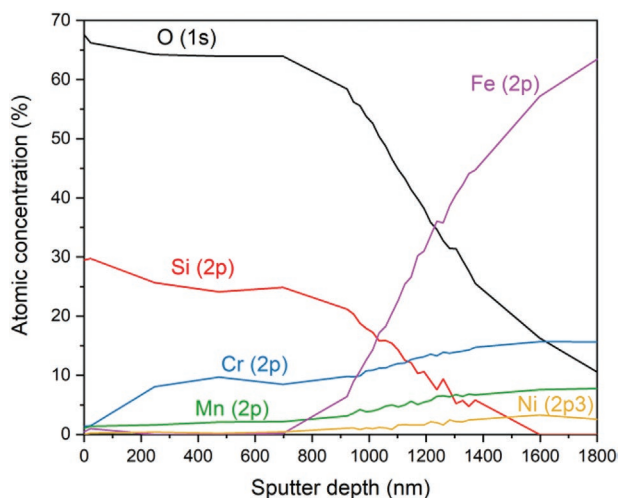


**Figure 9.** XPS depth profile of the Durazane 2250 coated AISI 304 steel after pyrolysis at 1000 °C for 1 h in air.

photoelectron spectroscopy (XPS) depth profile analysis was performed. The atomic concentration profile of the Durazane 2250 coated steel was measured up to 1800 nm depth (Figure 9).

In agreement with EDS analysis, XPS confirms Si (2p) and O (1s) as main elements of the Durazane 2250 based coating. After pyrolysis at 1000 °C for 1 h in air, no traces of N were detected, indicating its complete removal. Up to 500 nm, the relative atomic concentration of Cr increases significantly upon a slight decrease in the amounts of Si and O, confirming its diffusion from the AISI 304 substrate during pyrolysis. At above 500 nm and until 700 nm, the concentration of these elements remains almost unaltered. Up to 700 nm, the concentration of Mn (2p) within the coating is constant, confirming the faster diffusion of this element, already detected by EDS analysis. The depth range of 700 and up to 1600 nm characterizes a diffusion front, where the concentration of Fe (2p) steeply increases and the amounts of Si and O decrease. In addition, XPS analysis verifies the slightly increasing concentration of Cr (2p), Ni (2p3), and Mn (2p) with depth. Elements of the coating were also capable of diffusing beyond the estimated coating thickness (1200 nm, see Figure 8b). Therefore, Si is present up to 1600 nm, whereas 10 at% of O was detected at a depth of 1800 nm.

In comparison with the Durazane 2250 coating, the Yb50 coating shows a distinct microstructure, characterized by

smooth (1) and rough regions (2) with varying surface structure sizes of up to approximately 20 μm (Figure 10a).

EDS-analysis of region 1 also confirms Si and O as main elements within the coating, corresponding respectively to 32 and 24 at%, whereas approximately 2 at% of Yb were detected.

As discussed in Section 2.1, the pyrolysis of Durazane 1800 in air is strongly influenced by the modification with Yb, leading to a ceramic with an elemental composition of  $\text{SiC}_{0.07}\text{N}_{0.02}\text{O}_{1.93}\text{Yb}_{0.02}$ . Nevertheless, the detection of considerable amounts of Fe (15 at%), Cr (19 at%), and Mn (8 at%) within region 1 indicates the enhanced diffusion of these elements through the coating during pyrolysis. In contrast, region 2 is composed by mainly Fe (21 at%) and O (56 at%), whereas Si, Cr, and Mn account for 11, 10, and 2 at%, respectively. At higher magnifications (Figure 10b), whiskers are distinguishable, which have been commonly reported during the oxidation of fayalite ( $\text{Fe}_2\text{SiO}_4$ ). Gaballah et al. state that the oxidation of  $\text{Fe}_2\text{SiO}_4$  leads to the formation of a covering layer containing iron oxide and silica. The crystallization of silica develops with the relaxation of stress due to fracture, where hematite whiskers grow.<sup>[53]</sup> In this case, it is likely that the enhanced diffusion of iron and the incorporation of oxygen resulted in the formation of  $\text{Fe}_2\text{SiO}_4$ ,<sup>[9,10]</sup> followed by the growth of hematite whiskers. However, additional analyses are required to determine their nature.

The BSE analysis of the cross-section of the coating reveals a well-adhered and dense layer with a thickness of 1.2 μm (Figure 10c), whereas region 2 is restrained to the surface of the Yb50 coating, corresponding additionally to approximately 0.4 μm in thickness. This result supports the faster diffusion of transition metals from the substrate through the coating in comparison with Durazane 2250, as confirmed by XPS depth profile analysis (Figure 11).

The XPS depth profile of the Yb50 coated steel reveals that the main elements of this coating system correspond to Si (2p), O (1s), followed by Fe (2p), Cr (2p), and Mn (2p), in accordance with EDS analysis. Moreover, it confirms the complete removal of C and N from the starting Yb-modified precursor after pyrolysis at 1000 °C for 1 h in air. Up to a depth of 300 nm, a higher concentration of Fe (2p) was detected, whereas it decreases beyond this point up to 700 nm. This result is likely influenced by the higher Fe content within region 2, present at the surface of the coating (Figure 10c). From 300 until 700 nm, the concentration of other elements as Si, O, Cr, and Mn remain almost constant. Similarly to the Durazane 2250 coating, a diffusion front is estimated to

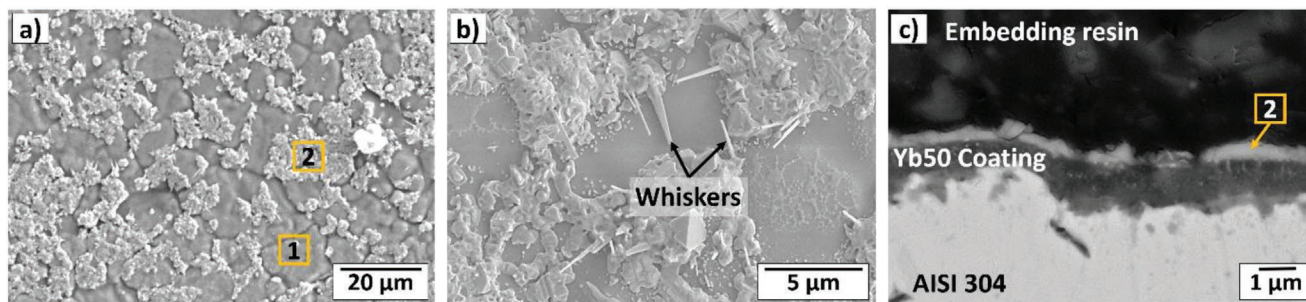


**Figure 10.** SEM/BSE analysis of the a,b) surface and c) cross-section of the Yb50 coating on AISI 304 after pyrolysis at 1000 °C for 1 h in air, and selected points for EDS analysis.

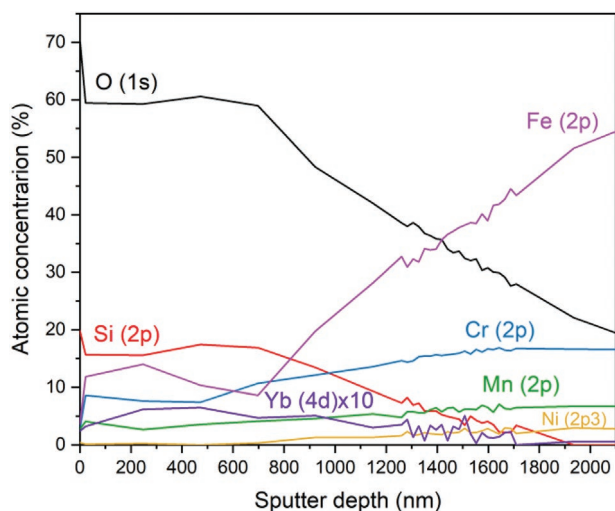


**Figure 11.** XPS depth profile of the Yb50-coated AISI 304 steel after pyrolysis at 1000 °C for 1 h in air.

start at 700 nm. On the one hand, the concentration of Fe steeply increases beyond this point, together with the detection of slightly increasing amounts of Cr, Ni (2p3), and Mn. On the other hand, the amounts of Si and O decrease gradually toward the substrate. Si was detected up to approximately 1900 nm, whereas 20 at% of O is still present up to 2100 nm, equivalent to a depth of 1600 nm in the Durazane 2250 coated steel. Despite the very low concentration of Yb (4d), its signal was detected up to approximately 1700 nm.

The differences in the mean atomic concentration of the Durazane 2250 and Yb50 coatings up to their respective total measured thickness of 1200 and 1600 nm are summarized in Table 4.

In comparison with the Durazane 2250 coating, considerably higher amounts of Fe, Cr, and Mn were detected within the Yb50 coating. Moreover, considering the thickness of both coatings and the clear formation of a diffusion front at above 700 nm in both systems, the faster diffusion of transition metals from the substrate into the Yb50 coating is evidenced.

At 1000 °C, Fe is capable of diffusing through SiO<sub>2</sub>-films at comparable rates to Cr, and faster than Mn, resulting in the

**Table 4.** Mean atomic concentration of the Durazane 2250 and Yb50 coatings on AISI 304 after pyrolysis at 1000 °C for 1 h in air.

	Atomic concentration [%]	
	Durazane 2250*	Yb50**
O (1s)	53.1	42.6
Si (2p)	18.7	8.9
Cr (2p)	9.8	13.3
Mn (2p)	3.7	5.2
Fe (2p)	13.7	28.0
Ni (2p3)	1.0	1.5
Yb (4d)	–	0.3

\*—up to 1200 nm; \*\*—up to 1600 nm.

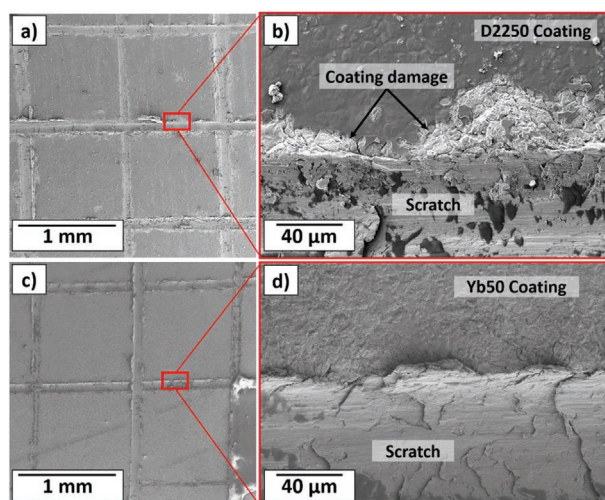


**Figure 12.** Cross-cut test with a) Durazane 2250 and c) Yb50 coatings on AISI 304 after pyrolysis at 1000 °C, 1 h in air, where (b) and (d) are respectively higher magnifications from (a) and (c).

reported composition,<sup>[54–56]</sup> whereas SiN<sub>x</sub> films are proven to be a more effective barrier against the diffusion of transition metals.<sup>[57,58]</sup> In this case, the high reactivity of the Yb50 coating with oxygen led to the faster formation of SiO<sub>2</sub>, whereas the slower oxidation of the Durazane 2250 coating is expected to have retarded the diffusion of elements from the substrate. The more distinct gradient structure of the Yb50 coating should lead to a decreased CTE mismatch to the AISI 304 steel substrate, thus avoiding the formation of cracks as detected for the Durazane 2250 coated steel (region 2, Figure 8a). To investigate the influence of the coating morphology on the adhesion to the steel substrate, the Durazane 2250 and Yb50 coatings were evaluated by cross-cut (Figure 12) and pull-off (Figure 13) tests.

Initially after the cross-cut test (Figure 12), the scratch patterns of the Durazane 2250 (a) and Yb50 (c) coatings appear very similar. However, at higher magnifications the partial spallation of the Durazane 2250 coating becomes clear (Figure 12b), which was estimated to be less than 5% of the tested area (GT 1). In contrast, SEM analysis of the surface of the Yb50

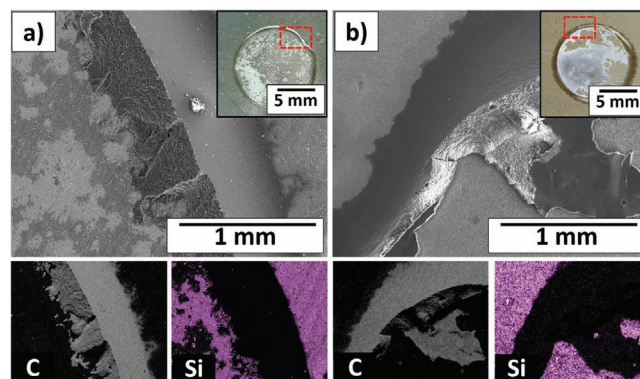


**Figure 13.** Pull-off tests of the a) Durazane 2250 and b) Yb50 coatings on AISI 304 and their respective Si and C EDS mappings after pyrolysis at 1000 °C for 1 h in air. C represents the adhesive and Si the coatings.

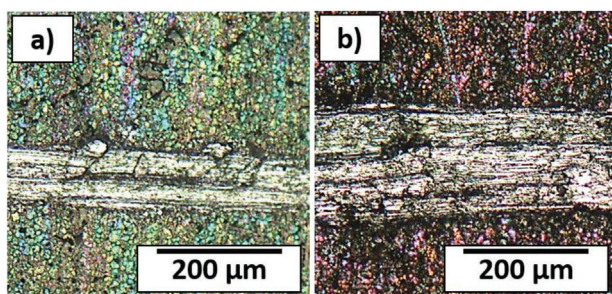


**Figure 14.** Optical microscopy of the a) Durazane 2250 and b) Yb50 coatings on AISI 304 pyrolyzed at 1000 °C for 1 h in air after the scratch test with a load of 10 and 38 N, respectively.

coating at higher magnification showed no signs of spallation (Figure 12d), thus corresponding to a GT 0 classification.

An adhesion of  $23.7 \pm 0.5$  MPa was measured for the Yb50 coating by pull-off test, slightly higher than  $19.5 \pm 2.9$  MPa, measured for the Durazane 2250 coating. The corresponding failure mechanism was investigated by SEM/EDS analysis (Figure 13), where the red dotted rectangle on the coated steel marks the analyzed region. The EDS element mappings of carbon and silicon indicate the epoxy resin and the coatings, respectively.

By comparing the SEM images of the coatings with their respective EDS mappings, Si is still detected within the tested areas of both samples after the pull-off tests. However, within the detached area the Durazane 2250 coating remained only partially adhered to the surface of the steel, as the dark regions with neither C nor Si represent the steel substrate (Figure 13a) and evidence an adhesion failure. In contrast, the analysis of the Yb50 coating indicates no signs of damage (Figure 13b). In this case, the epoxy resin failed by cohesion. As supporting information to the adhesion tests and as a direct evidence of the hardness of the thin coatings, scratch tests determined the necessary load to damage the Durazane 2250 (a) and the Yb50 (b) coating on the AISI 304 steel (Figure 14).

A load of 10 N resulted in a scratch width of 86 µm on the surface of the Durazane 2250 coating (Figure 14a), whereas the Yb50 coating was capable of withstanding loads of up to 38 N before failing, resulting in a scratch width of 157 µm (Figure 14b).

Despite the decreased hardness associated to  $\text{FeSi}_x\text{O}_y$  coatings (up to 9.6 GPa)<sup>[59,60]</sup> in comparison with Durazane 2250 coatings (12 GPa, 1000 °C in air),<sup>[11]</sup> dense and thin  $\text{Cr}_2\text{O}_3$  films exhibit an increased hardness of up to 32 GPa and are capable to withstand a critical load of 70 N.<sup>[61,62]</sup> Thus, the superior adhesion and scratch tolerance of the Yb50 coatings benefits from the enhanced diffusion of transition metals from the steel, leading to a distinct gradient as confirmed by EDS elemental analysis (Figure 10) and XPS depth profiling (Figure 11).

The protective effect of the Durazane 2250 and the Yb50 coatings was evaluated during dry and wet oxidation tests in air. Since no signs of degradation were detected after dry oxidation with coated steel samples at 900 °C for 15 h in air, the oxidation temperature was increased to 1000 °C (Figure 15).

Already after 5 h of oxidation at 1000 °C, slight signs of degradation are visible for both Durazane 2250 and Yb50 coated steel samples. As the oxidation time increases to 10 and 15 h,

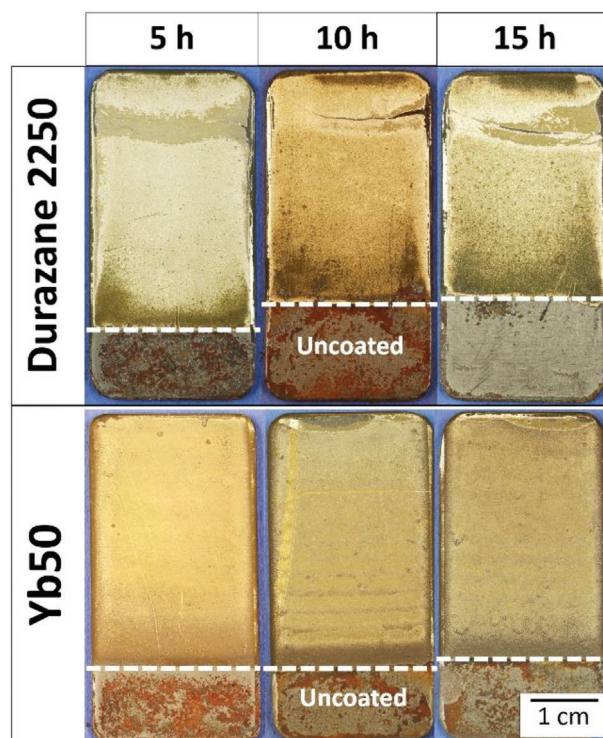


**Figure 15.** Oxidation of Durazane 2250 and Yb50 coated AISI 304 at 1000 °C in air for 5, 10, and 15 h.

more defects are visible for the Durazane 2250 coated sample, especially at the corners of the coating. These regions correspond respectively to thinner and thicker coatings caused by the dip-coating process and are usually the first to fail. At thinner coating regions the insufficient thickness enables the faster oxidation of the substrate, whereas at thicker coating regions, spallation may occur.<sup>[13,14]</sup> In contrast, the Yb50 coated system seems more stable against oxidation as the benchmark coating based on Durazane 2250.

In comparison with dry oxidation,  $\text{H}_2\text{O}_{(v)}$  is capable of diffusing more rapidly through  $\text{SiO}_2$  films than  $\text{O}_2$ ,<sup>[1,7,24,25]</sup> therefore the enhanced oxidation of the Yb50 and Durazane 2250 coated steels can be expected due to exposure to moisture containing atmospheres at 1000 °C for 15 h as described in Section 4.5. SEM/EDS analysis of the Durazane 2250 and the Yb50 coatings on AISI 304 after wet oxidation provide more information on their protection mechanisms, shown respectively in Figures 16 and 17.

As discussed previously, the resulting coatings are always thinner closer to the uncoated region of the steel substrate, because of the dip-coating process. Therefore, the oxidation of the coated AISI 304 steel starts at the uncoated and thinner coating regions with the formation of a protective  $\text{Cr}_2\text{O}_3$ -scale. After 2 h exposure at 1000 °C, the breakdown point is achieved, which leads to the rapid growth of the chromia scale and to the formation of a non-protective  $\text{Fe}_2\text{O}_3$ -scale upon the depletion of Mn and Cr. Beyond this point, the  $\text{Cr}_2\text{O}_3$ -layer is no longer capable of protecting the steel substrate against oxidation.<sup>[1,2,51]</sup> During exposure for 15 h at 1000 °C, the damage to the surface of the Durazane 2250 coated steel progressed (Figure 16a),

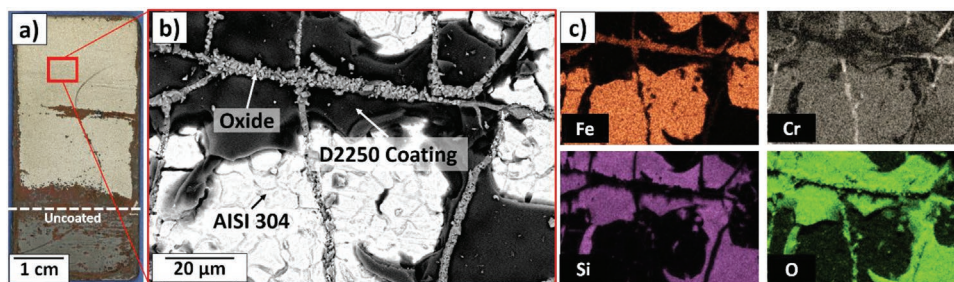


**Figure 16.** a) Picture, b) SEM/BSE image, and c) EDS mapping of the surface of the Durazane 2250 coated AISI 304 steel after wet oxidation in moist flowing air at 1000 °C for 15 h ( $P = 1$  atm,  $P_{\text{H}_2\text{O}} = 0.3$  atm, and  $v = 10$  mm s $^{-1}$ ).

which is mainly attributed to the faster diffusion of water vapor through the SiO<sub>2</sub>-based coating. Interestingly, the SEM/BSE analysis of the Durazane 2250 coated steel within the red dotted rectangle, where no signs of oxidation are visible in Figure 16a, reveals the spallation of the coating after testing (Figure 16b). In this case, the CTE mismatch between the Mn<sub>x</sub>Cr<sub>y</sub>O-scale (region 2, Figure 8) and the SiO<sub>2</sub>-derived coating are likely the cause for spallation, as confirmed by the Cr and Fe mappings of Figure 16c. The varying intensities of these elements detected within this region evidence different compositions, which may correspond to either Fe<sub>2</sub>O<sub>3</sub> or Cr<sub>2</sub>O<sub>3</sub>, representing an advanced stage of oxidation of AISI 304. The CTE mismatch between the SiO<sub>2</sub>-based coating and the metal oxides led to the generation of stresses within the coating during cooling,<sup>[59,63]</sup> thus resulting in its spallation. In contrast, the Yb50 coating remained undamaged (Figure 17a,b), indicating the beneficial effect of the modification of Durazane 1800 with Yb. In this case, the formation of β-Yb<sub>2</sub>Si<sub>2</sub>O<sub>7</sub> was proved after pyrolysis of the Yb50 precursor at 1000 °C in air, known for its high stability in moisture containing environments at high temperatures. Based on the work of Opila et al.,<sup>[64]</sup> the interaction between SiO<sub>2</sub> and water vapor leads to the formation of volatile silicon hydroxide (Si(OH)<sub>4</sub>). The critical temperature for silica volatilization, where increased corrosion rates are reported, is dependent on the temperature and water vapor partial pressure ( $p_{\text{H}_2\text{O}}$ ). In our case, a critical temperature close to 1000 °C can be expected due to the high  $p_{\text{H}_2\text{O}}$  (0.3 atm), besides the higher diffusion rates of H<sub>2</sub>O through SiO<sub>2</sub> films in comparison with molecular oxygen (O<sub>2</sub>),<sup>[24]</sup> thus contributing to the degradation of the coatings. However, in compounds from the system Yb–Si–O as ytterbium silicates, the stability of bound SiO<sub>2</sub> is

significantly increased and very low corrosion rates are reported up to 1450 °C in wet environments.<sup>[30]</sup> Therefore, it is likely that the diffusion of water vapor through the Yb50 coating is hindered upon interaction with Yb–Si–O phases present within it, which is supported by the higher stability of the Yb50 coatings in wet environments in comparison with Durazane 2250. Another beneficial effect is the enhanced interaction between Yb50 and the AISI 304 steel substrate and the formation of a gradient coating, as it avoided the formation of cracks within the coating as reported for Durazane 2250. Consequently, a better performance of the Yb50 coated steel is to be expected during thermal shock tests. **Figure 18** depicts both coating types on AISI 304 after 1, 3, 5, and 6 cycles between 1000 and 20 °C.

Already after 1 cycle, defects are visible on the surface of the Durazane 2250 coated steel, whereas the Yb50 coating remained intact. As the test progressed (3 cycles), the initial defective region oxidized completely and increased in size, leading to the complete failure of the Durazane 2250 coating after 5 cycles. Although the Yb50 coating also failed after 6 cycles, only slight signs of oxidation are visible on its surface up to 5 cycles. Moreover, undamaged coated areas were still present after 9 cycles. During thermal cycling, the coatings and especially the steel substrate go through a rapid expansion when exposed to 1000 °C, followed by a rapid contraction during quenching in water at 20 °C. Due to the CTE mismatch between the coatings and the steel substrate, their spallation is inevitable. Therefore, a reduced CTE mismatch between the AISI 304 steel substrate and Yb50 coating is expected due to the enhanced diffusion of transition metals in comparison with the Durazane 2250 coating, thus leading to an increased stability during thermal cycling. In the latter case, the faster failure of the coating system is additionally attributed to the CTE difference between regions 1 and 2 (refer to Figure 8), as previously discussed for wet oxidation.

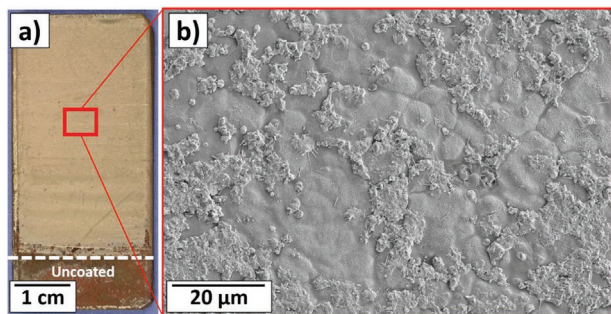


**Figure 17.** a) Picture and b) SEM analysis of the surface of the Yb50 coated AISI 304 steel after wet oxidation in moist flowing air at 1000 °C for 15 h ( $P = 1$  atm,  $P_{\text{H}_2\text{O}} = 0.3$  atm, and  $v = 10$  mm s $^{-1}$ ).

### 3. Conclusion

In this work, the chemical modification of silazanes with ytterbium (Yb) was successfully carried out in order to increase the stability of silazane-based ceramic coatings in very harsh hot gas corrosion environments like gas turbines and exhaust lines at temperatures above 1200 °C. Hence, the hot gas corrosion stable phase β-Yb<sub>2</sub>Si<sub>2</sub>O<sub>7</sub> was generated by the reaction of NH groups of the oligosilazane Durazane 1800 with Yb(Ap<sup>TMS</sup>)<sub>3</sub>, followed by pyrolysis of the resulting Yb-modified silazanes in air.

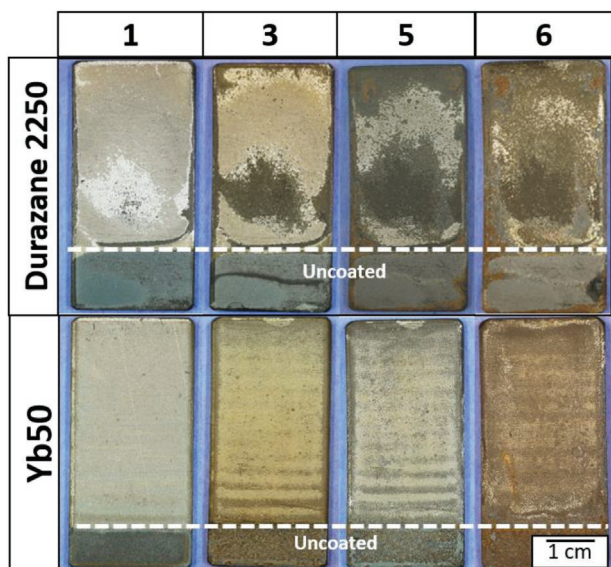


**Figure 18.** Thermal shock tests of Durazane 2250 and Yb50 coated AISI 304 steel after annealing at 1000 °C for 1 h in air and subsequent quenching in water at 20 °C.

The influence of the incorporation of Yb on the chemical structure and pyrolysis behavior of silazanes was thoroughly studied by varying the Si to Yb ratio within the modified precursors. Thereafter, the Yb-modified silazanes were applied as protective coatings onto AISI 304. The best resulting coated system was tested against oxidation in dry and wet atmospheres up to 15 h at 1000 °C, simulating combustion environments. A detailed discussion of its microstructure and protection mechanism is provided as well as a comparison to the benchmark silazane Durazane 2250.

FTIR, TG, and elemental analyses of the Yb-modified silazanes confirmed their remarkable interaction with oxygen, thus enabling an increased degree of cross-linking at already low temperatures by the formation of Si–O–Si bonds and the substitution of C and N from the oligosilazane Durazane 1800 by oxygen and influencing its pyrolysis behavior. Consequently, pyrolysis at 1000 °C in air led to the crystallization of SiO<sub>2</sub> as  $\alpha$ -cristobalite and  $\alpha$ -quartz and  $\beta$ -Yb<sub>2</sub>Si<sub>2</sub>O<sub>7</sub>, favored at higher Yb contents. Based on the elemental composition of Yb50

after pyrolysis (SiC<sub>0.07</sub>N<sub>0.02</sub>O<sub>1.93</sub>Yb<sub>0.02</sub>) and the corresponding refined XRD data, a total conversion of 37 mol% atomic Yb into  $\beta$ -Yb<sub>2</sub>Si<sub>2</sub>O<sub>7</sub> was calculated, corresponding to 2.52 wt% of the ceramic composition.

In comparison with the benchmark Durazane 2250 coatings for AISI 304, at already very low Yb contents, Yb50 coatings exhibited a similar oxidation protection after pyrolysis at 1000 °C in air. SEM/EDS and XPS depth profile analyses revealed in both cases a well-adhered and dense SiO<sub>2</sub>-based layer with a thickness of 1.2  $\mu$ m. The positive influence of the modification of silazanes with Yb was confirmed by the decreased CTE mismatch to the stainless steel, caused by the enhanced diffusion of transition metals into the Yb50 coating, thus hindering the formation of cracks as seen for the Durazane 2250 coating. Consequently, it exhibited a superior adhesion and scratch tolerance as determined by cross-cut (GT 0), pull-off (23.7  $\pm$  0.5 MPa), and scratch tests (38 N) in comparison with the Durazane 2250-based coating (i.e., GT 1; 19.5  $\pm$  2.9 MPa; 10 N). In addition, the Yb50-coated AISI 304 steel was able to withstand up to 9 thermal cycles between 1000 and 20 °C. In contrast to the Durazane 2250 coated AISI 304 steel, the Yb50-coated system showed only minor damages after oxidation in dry and wet environments up to 15 h at 1000 °C. Especially in wet environments, the better performance of the Yb50 coating is attributed to the presence of Yb–Si–O phases, which retarded the diffusion of water vapor through the coating and attenuated the effects related to oxidation. Therefore, we conclude that the modification of silazanes with Yb is a suitable approach to increase the stability of silazane-based ceramic coatings in combustion environments via generation of stable silicate phases and the deposition of coatings with increased mechanical and oxidation stability.

## 4. Experimental Section

**Materials:** All syntheses were carried out in purified argon atmosphere to prevent any contact with air by using the standard Schlenk technique. The polysilazanes Durazane 1800, Durazane 1033, and Durazane 2250 were obtained from Merck KGaA (Germany). HTTS was synthesized by the selective cross-linking of Durazane 1800, according to the procedure described by Flores et al.<sup>[50]</sup> 4-methyl-2-((trimethylsilyl)amino)pyridine (Ap<sup>TMS</sup>H) was synthesized according to a procedure reported elsewhere.<sup>[34]</sup> Ytterbium (III) chloride (YbCl<sub>3</sub>, anhydrous, 99.9%) was

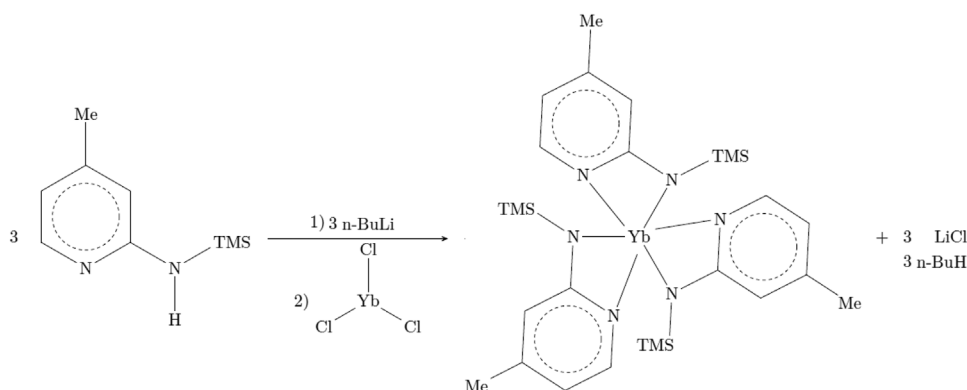


**Figure 19.** Reaction scheme for the preparation of the complex Yb(Ap<sup>TMS</sup>)<sub>3</sub>.

**Table 5.** Composition of the Yb-modified polysilazanes.

Sample	Si:Yb ratio	Durazane 1800 + 3 wt% DCP [wt%]
Yb100	100	90
Yb50	50	82
Yb25	25	70

purchased from abcr GmbH (Germany). Tetrahydrofuran (THF), diethylether (Et<sub>2</sub>O), toluene, and *n*-hexane (extra dry over molecular sieve, AcroSeal) and *n*-butyl lithium (BuLi, 2.5 M in hexane) were obtained from Fisher Scientific GmbH (Germany) and used without further purification. Dicumyl peroxide (DCP, 98%) was purchased from Sigma-Aldrich Co. LLC. (Germany) and used as received. All chemicals used in the synthesis of the modified silazanes were handled in a nitrogen filled glovebox (MBraun, MB-200G, <1 ppm H<sub>2</sub>O/O<sub>2</sub>). Ytterbium (III) oxide (Yb<sub>2</sub>O<sub>3</sub> REacton, 99.9%) and silicon dioxide (SiO<sub>2</sub>, 99.5%) were acquired from Alfa Aesar GmbH & Co. KG, Germany. Ytterbium disilicate (Yb<sub>2</sub>Si<sub>2</sub>O<sub>7</sub>, 99.98%) was purchased from Treibacher Industries AG, Austria.

**Synthesis of the Ytterbium-Modified Polysilazane: Preparation of the Ytterbium Complex (Yb(Ap<sup>TMS</sup>)<sub>3</sub>):** In a typical reaction, BuLi (30 mL, 75 mmol) was added dropwise to a solution of Ap<sup>TMS</sup>H (13.5 g, 75 mmol) dissolved in Et<sub>2</sub>O (50 mL). After 30 min of vigorous stirring, the resulting solution was poured into an addition funnel connected to a Schlenk containing YbCl<sub>3</sub> (6.99 g, 25 mmol) dispersed in Et<sub>2</sub>O (30 mL). The activated ligand was added dropwise to the YbCl<sub>3</sub> solution and the mixture was further stirred overnight leading to the formation of a white precipitate (lithium chloride, LiCl). The Et<sub>2</sub>O solvent was removed under vacuum (30 °C, 10<sup>-1</sup> mbar). *n*-hexane (150 mL) was then added to the Schlenk in order to extract the metal complex from LiCl. Finally, the solvent removal at 30 °C and 10<sup>-1</sup> mbar led to a moisture and air sensitive yellow solid. The corresponding reaction scheme is shown in **Figure 19**.

**Preparation of Ytterbium-Modified Polysilazanes:** Various precursors were synthesized with different Si:Yb ratios as shown in **Table 5**. Therefore, a toluene solution of the ytterbium complex was added dropwise to the corresponding amount of Durazane 1800, also dissolved in toluene, which was subsequently vigorously stirred overnight. The expected reaction scheme is shown in **Figure 20**. For structural analyses of the resulting precursors before pyrolysis, the solvent was removed after synthesis, yielding a viscous yellow liquid. Additionally, a sample with the molar ratio of 10 Si to 1 Yb (Yb10) was synthesized to emphasize the effects related to the incorporation of Yb. Otherwise, 3 wt% DCP, regarding the oligosilazane, was added to promote the cross-linking of the modified precursors via hydrosilylation and polymerization reactions, thus increasing their ceramic yield upon pyrolysis.<sup>[37,65,66]</sup> For coating purposes, the procedure was set up in a way to obtain a final

20 wt% Yb-modified polysilazane solution, which was stored inside the glovebox.

**Characterization of the Ytterbium-Modified Polysilazanes:** All polymer samples are sensitive to moisture and air. Therefore, their preparation was carried out inside the glovebox. The chemical structure of the modified precursors was investigated by Fourier transform infrared spectroscopy (FTIR), using a Tensor 27 (Bruker Corporation, USA) equipped with an attenuated total reflectance (ATR) unit, recorded within the range 400–4000 cm<sup>-1</sup>. A total of 16 scans with a resolution of 4 cm<sup>-1</sup> were performed. Solid state <sup>13</sup>C CP MAS and <sup>29</sup>Si MAS nuclear magnetic resonance (NMR) spectra were recorded on an Avance 400 spectrometer (Bruker Corporation, USA) using 3.5 mm Bruker probes and spinning frequencies of 10, 12.5, or 20 kHz. <sup>13</sup>C CP MAS measurements were recorded with cross-polarization in the <sup>1</sup>H channel to transfer magnetization from <sup>1</sup>H to <sup>13</sup>C. Chemical shift values were referenced to tetramethylsilane. Only for NMR purposes, the oligosilazane Durazane 1033 (showing only SiH, NH, and CH<sub>3</sub> functional groups) was modified with the Yb-complex in a 10 Si to 1 Yb ratio in order to avoid possible side reactions of BuLi with the vinyl groups of Durazane 1800, thus hindering the correct peak assignment of the obtained spectra. After the synthesis, an adequate amount of BuLi was added in order to precipitate and remove the Ap<sup>TMS</sup>H released during the reaction as Ap<sup>TMS</sup>Li. The resulting ML-Yb10 sample was a yellow solid. Elemental analyses were performed by Mikroanalytisches Labor Pascher in Remagen, Germany. TGA were carried out using an STA 449 F5 Jupiter (Netzsch GmbH & Co. Holding KG, Germany) at 5 K min<sup>-1</sup> and up to 1000 °C in synthetic air (80/20 vol% N<sub>2</sub>/O<sub>2</sub>). The crystallization effects of the resulting ceramics were investigated by FTIR and X-ray diffractometry (XRD). For a matter of comparison, the FTIR spectra of Yb<sub>2</sub>O<sub>3</sub>, SiO<sub>2</sub> and Yb<sub>2</sub>Si<sub>2</sub>O<sub>7</sub> were also measured. XRD analysis was carried out in a D8 ADVANCE (Bruker Corporation, USA) using monochromatic CuKα radiation. The crystalline phases were identified using the PDF-4+ 2016 structural database, whereas the refinement and quantification of the resulting diffractograms was performed in Topas v. 4.2.

**Preparation of the Coatings:** For the preparation of the coatings, AISI 304 stainless steel sheets were cut into 25 × 50 mm substrates, which were cleaned in an acetone ultrasonic bath for 25 min to remove any superficial impurities. The steel substrates were dip-coated inside the glovebox using a RDC 10 dip-coater (Bungard Elektronik GmbH & Co. KG, Germany) with a hoisting speed of 0.5 m min<sup>-1</sup>. The coated substrates were pyrolyzed in an N41/H furnace (Nabertherm GmbH, Germany) at 1000 °C for 1 h in air and heating rate of 5 K min<sup>-1</sup>. For a matter of comparison, Durazane 1800 + 3 wt% DCP, HTTS, and Durazane 2250 silazane-based coatings were likewise processed.

**Characterization of the Coatings:** After pyrolysis, only the best coated samples were characterized. Their microstructure was evaluated using a scanning electron microscope (SEM) Gemini Sigma 300 VP (Carl Zeiss AG, Germany), coupled with an EDAX Octane Elect SDD, used for energy-dispersive X-ray spectroscopy (EDS).

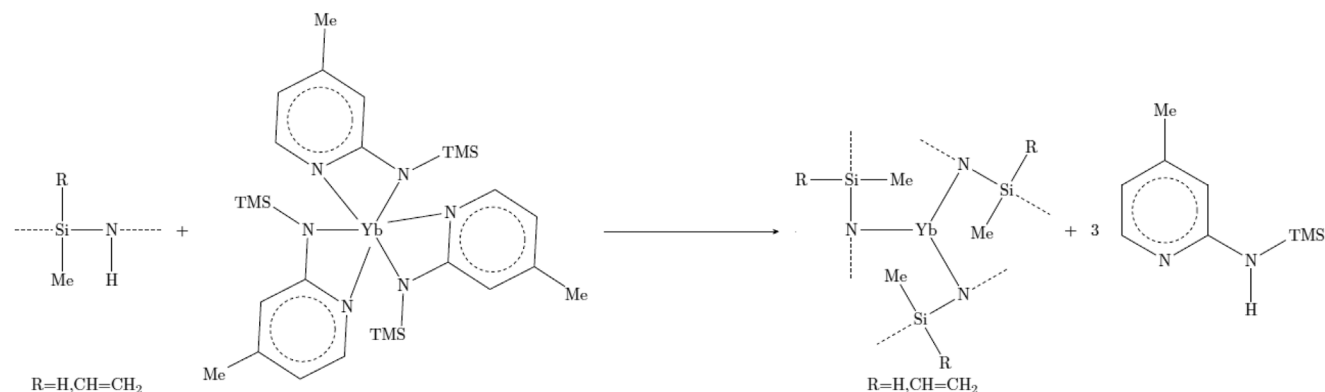


**Figure 20.** Expected reaction scheme for the preparation of Yb-modified Durazane 1800.

X-ray photoelectron spectroscopy (XPS) ion sputtering depth profiling across the coating interface was performed at Physical Electronics GmbH in Ismaning (Germany) using a Phi Quantum 2000 spectrometer. The source of X-rays was a monochromatic Al-K $\alpha$  lamp at 1486.68 eV photon energy and a beam width of 100  $\mu\text{m}$ . The samples were evaluated using O 1s, Si 2p, Cr 2p, Mn 2p, Fe 2p, Ni 2p<sub>3/2</sub>, and Yb 4d regions at a 45° take-off angle up to a sputter depth of 2.2  $\mu\text{m}$  in a 1.4  $\times$  0.4 mm raster area. The analysis was performed by ion peeling with an Ar ion beam (2 kV) at a material removal rate of 22 nm min<sup>-1</sup>.

The adhesion of the coatings was investigated by cross-cut and pull-off tests after pyrolysis. The cross-cut tape test was performed by scratching the surface of the coated samples manually with a cutting tool (ZCC 2087, MTV Messtechnik oHG, Germany) to obtain a 90° angle grid pattern according to the standard DIN EN ISO 2409. Afterward, a suitable tape was glued onto the surface of the coated samples and removed after 5 min in a 60° angle. The coatings were classified according to the area damaged during testing (i.e., GT 0: 0%, GT 1: <5%, GT 2: 5–15%, GT 3: 15–35%, GT 4: 35–65%, and GT 5: >65%). The pull-off tests were performed using a DeFelsko PosiTest AT-A (USA), according to the ASTM D4541. Thus, aluminum dollies with  $\varnothing$  10 mm were glued onto the surface of the coated steel samples using a two-component epoxy resin Loctite EA 9466 (Henkel Central Eastern Europe GmbH, Austria). The resin was cured at 110 °C for 1 h in air prior to the test, resulting in a tensile strength of 32 MPa. Subsequently, the dollies were pulled perpendicularly with a constant force of 1 MPa s<sup>-1</sup>. The tensile strength necessary to detach the dollies was recorded. The values reported herein are an average of five measurements. The failure mechanism of the coating systems was determined by SEM/EDS analysis.

As a supporting information to the adhesion tests, scratch tests were performed using a Lineartester 249 (Erichsen GmbH & Co. KG, Germany) with varying load ranging from 5 to 40 N. Therefore, a testing rod 15/570 ( $\varnothing$  1.0 mm) was used, according to the standard ISO 1518-1. The load necessary to damage the surface of the coatings was determined by optical microscopy in Axiotech HAL 100 (Carl Zeiss AG, Germany).

Dry oxidation tests with the coated steel samples were carried out in the Nabertherm N41/H furnace at 1000 °C in air, heating rate of 5 K min<sup>-1</sup> and holding times of 5, 10, 15 h to evaluate their protective effect against oxidation of the AISI 304 substrate. Additionally, wet oxidation was performed in flowing water vapor atmosphere, consisting of a mixture of water vapor and synthetic air ( $P_{\text{H}_2\text{O}} = 0.3 \text{ atm}$ ,  $P = 1 \text{ atm}$ ) with an average flow speed of 10 mm s<sup>-1</sup>. In this case, the coated samples were placed in a tubular Al<sub>2</sub>O<sub>3</sub> furnace model 0118T (Clasic CZ Ltd., Czech Republic), which was heated up to 1000 °C (5 K min<sup>-1</sup>) and held isothermally for 15 h. Thermal shock tests evaluated the stability of the coated systems upon thermal cycling in air. Therefore, a B150 furnace (Nabertherm GmbH, Germany) was held isothermally at 1000 °C. The coated systems were placed inside the heated furnace and annealed for 1 h before quenching in a water bath at 20 °C. Afterwards, the samples were allowed to dry at 110 °C for 30 min and loaded back into the heated furnace for the next cycle. A total of nine cycles were performed.

## Acknowledgements

The authors would like to thank DFG (Deutsche Forschungsgemeinschaft) for the financial support within the project 453000562 (MO 851/20) and DAAD (German Academic Exchange Service, Project-ID 57320317) for the financial support.

Open access funding enabled and organized by Projekt DEAL.

## Conflict of Interest

The authors declare no conflict of interest.

## Data Availability Statement

The data that support the findings of this study are available from the corresponding author upon reasonable request.

## Keywords

combustion environments, environmental barrier coating, polymer derived ceramics, silazanes, ytterbium silicate

Received: March 8, 2021

Revised: April 20, 2021

Published online: June 9, 2021

- [1] A. M. Huntz, A. Reckmann, C. Haut, C. Sév erac, M. Herbst, F. C. T. Resende, A. C. S. Sabioni, *Mater. Sci. Eng. A* **2007**, *447*, 266.
- [2] K. A. Habib, M. S. Damra, J. J. Saura, I. Cervera, J. Bell es, *Int. J. Corros.* **2011**, *1*, 1.
- [3] W. J. Nowak, *J. Anal. At. Spectrom.* **2017**, *32*, 1730.
- [4] S. Cruchley, H. Evans, M. Taylor, *Mater. High Temp.* **2016**, *33*, 465.
- [5] A. Sato, Y.-L. Chiu, R. C. Reed, *Acta Mater.* **2011**, *59*, 225.
- [6] G. Koch, J. Varney, N. Thompson, O. Moghissi, M. Gould, J. Payer, *International Measures of Prevention, Application, and Economics of Corrosion Technologies Study* (Ed: G. Jacobson), NACE International, Houston, Texas, USA **2016**, pp 1–72.
- [7] G. H. Meier, F. S. Pettit, K. Onal, *Interaction of Steam/Air Mixtures-With Turbine Airfoil Alloys and Coatings*, AGSTR Semi-Annual Report, University of Pittsburgh, **2002**.
- [8] J. R. Miranda, M. A. S anchez, E. G. Garc a, D. Y. M. Velazquez,  . J. de Morales Ram rez, in *Characterization of Metals and Alloys* (Eds: R. P erez Campos, A. Contreras Cuevas, R. A. Esparza Mu oz), Springer International Publishing, Switzerland **2017**, pp. 109–116.
- [9] F. J. P erez, M. P. Hierro, M. C. Carpintero, C. G omez, F. Pedraza, *Surf. Coat. Technol.* **2002**, *160*, 87.
- [10] M. Zandrahimi, J. Vatandoost, H. Ebrahimifar, *Oxid. Met.* **2011**, *76*, 347.
- [11] M. G unthner, K. Wang, R. K. Bordia, G. Motz, *J. Eur. Ceram. Soc.* **2012**, *32*, 1883.
- [12] M. G unthner, T. Kraus, A. Dierdorf, D. Decker, W. Krenkel, G. Motz, *J. Eur. Ceram. Soc.* **2009**, *29*, 2061.
- [13] M. G unthner, T. Kraus, W. Krenkel, G. Motz, A. Dierdorf, D. Decker, *Int. J. Appl. Ceram. Technol.* **2009**, *6*, 373.
- [14] M. G unthner, A. Sch utz, U. Glatzel, K. Wang, R. K. Bordia, O. Grei el, W. Krenkel, G. Motz, *J. Eur. Ceram. Soc.* **2011**, *31*, 3003.
- [15] K. Wang, M. G unthner, G. Motz, R. K. Bordia, *J. Eur. Ceram. Soc.* **2011**, *31*, 3011.
- [16] G. S. Barroso, W. Krenkel, G. Motz, *J. Eur. Ceram. Soc.* **2015**, *35*, 3339.
- [17] M. Lenz Leite, G. Barroso, M. Parchoviansk y, D. Galusek, E. Ionescu, W. Krenkel, G. Motz, *J. Eur. Ceram. Soc.* **2017**, *37*, 5177.
- [18] A. Morlier, S. Cros, J.-P. Garandet, N. Alberola, *Thin Solid Films* **2012**, *524*, 62.
- [19] P. Colombo, G. Mera, R. Riedel, G. D. Sorar , *J. Am. Ceram. Soc.* **2010**, *93*, 1805.
- [20] G. Motz, T. Schmalz, S. Trassl, R. Kempe, *Oxidation Behavior of SiCN Materials. In Design, Processing and Properties of Ceramic Materials from Preceramic Precursors* (Ed: S. Bernard), Nova Science Publishers Inc., UK **2011**, pp. 15–36.
- [21] L. An, Y. Wang, L. Bharadwaj, L. Zhang, Y. Fan, D. Jiang, Y. Sohn, V. H. Desai, J. Kapat, L. C. Chow, *Adv. Eng. Mater.* **2004**, *6*, 337.

- [22] P. Greil, *J. Am. Ceram. Soc.* **1995**, *78*, 835.
- [23] O. Goerke, E. Feike, T. Heine, A. Trampert, H. Schubert, *J. Eur. Ceram. Soc.* **2004**, *24*, 2141.
- [24] N. S. Jacobson, *J. Am. Ceram. Soc.* **1993**, *76*, 3.
- [25] B. E. Deal, A. S. Grove, *J. Appl. Phys.* **1965**, *36*, 3770.
- [26] H. Klemm, *J. Eur. Ceram. Soc.* **2002**, *22*, 2735.
- [27] D. S. Fox, E. J. Opila, Q. G. N. Nguyen, D. L. Humphrey, S. M. Lewton, *J. Am. Ceram. Soc.* **2003**, *86*, 1256.
- [28] N. Maier, K. G. Nickel, G. Rixecker, *J. Eur. Ceram. Soc.* **2007**, *27*, 2705.
- [29] Y. Wang, J. Liu, *J. Eur. Ceram. Soc.* **2009**, *29*, 2163.
- [30] H. Klemm, *J. Am. Ceram. Soc.* **2010**, *93*, 1501.
- [31] K. N. Lee, D. S. Fox, N. P. Bansal, *J. Eur. Ceram. Soc.* **2005**, *25*, 1705.
- [32] A. J. Fernández-Carrión, M. D. Alba, A. Escudero, A. I. Becerro, *J. Solid State Chem.* **2011**, *184*, 1882.
- [33] G. Bocquillon, C. Chateau, C. Loriers, J. Loriers, *J. Solid State Chem.* **1977**, *20*, 135.
- [34] R. Kempe, P. Arndt, *Inorg. Chem.* **1996**, *35*, 2644.
- [35] M. Zaheer, T. Schmalz, G. Motz, R. Kempe, *Chem. Soc. Rev.* **2012**, *41*, 5102.
- [36] M. Zaheer, G. Motz, R. Kempe, *J. Mater. Chem.* **2011**, *21*, 18825.
- [37] G. Glatz, T. Schmalz, T. Kraus, F. Haarmann, G. Motz, R. Kempe, *Chem. - Eur. J.* **2010**, *16*, 4231.
- [38] E. Ionescu, B. Papendorf, H. J. Kleebe, H. Breitzke, K. Nonnenmacher, G. Buntkowsky, R. Riedel, *J. Eur. Ceram. Soc.* **2012**, *32*, 1873.
- [39] S. M. Sachau, M. Zaheer, A. Lale, M. Friedrich, C. E. Denner, U. B. Demirci, S. Bernard, G. Motz, R. Kempe, *Chem. - Eur. J.* **2016**, *22*, 15508.
- [40] M. Zaheer, J. Hermannsdörfer, W. P. Kretschmer, G. Motz, R. Kempe, *ChemCatChem* **2014**, *6*, 91.
- [41] J. Yuan, M. Galetz, X. G. Luan, C. Fasel, R. Riedel, E. Ionescu, *J. Eur. Ceram. Soc.* **2016**, *36*, 3021.
- [42] D. Forberg, T. Schwob, M. Zaheer, M. Friedrich, N. Miyajima, R. Kempe, *Nat. Commun.* **2016**, *7*, 13201.
- [43] J. Schuhmacher, F. Berger, M. Weinmann, J. Bill, F. Aldinger, K. Müller, *Appl. Organomet. Chem.* **2001**, *15*, 809.
- [44] J. Seitz, J. Bill, N. Egger, F. Aldinger, *J. Eur. Ceram. Soc.* **1996**, *16*, 885.
- [45] R. Choong Kwet Yive, R. J. P. Corriu, D. Leclercq, P. Mutin, A. Vioux, *New J. Chem.* **1991**, *15*, 85.
- [46] M. Seifert, N. Travitzky, W. Krenkel, G. Motz, *J. Eur. Ceram. Soc.* **2014**, *34*, 1913.
- [47] P. Launer, B. Arkles, in *Silicone Compounds Register and Review*, Petrarch Systems, USA **2008**, pp. 223–226.
- [48] M. Díaz, C. Pecharrmán, F. del Monte, J. Sanz, J. E. Iglesias, J. S. Moya, C. Yamagata, S. Mello-Castanho, *Chem. Mater.* **2005**, *17*, 1774.
- [49] H. Salmang, H. Scholze, *Keramik* (Ed: R. Telle), 7th ed., Springer-Verlag, Berlin Heidelberg **2007**.
- [50] O. Flores, T. Schmalz, W. Krenkel, L. Heymann, G. Motz, *J. Mater. Chem. A* **2013**, *48*, 15406.
- [51] R. Guillamet, J. Lopitiaux, B. Hannoyer, M. Lenglet, *J. Phys., Colloq.* **1993**, *03*, C9.
- [52] F. H. Stott, F. I. Wei, C. A. Enahoro, *Mater. Corros.* **1989**, *40*, 198.
- [53] I. Gaballah, S. El Raghy, C. Gleitzer, *J. Mater. Sci.* **1978**, *13*, 1971.
- [54] H. G. Francois-Saint-Cyr, F. A. Stevie, J. M. McKinley, K. Elshot, L. Chow, K. A. Richardson, *J. Appl. Phys.* **2003**, *94*, 7433.
- [55] K. Saga, R. Ohno, D. Shibata, S. Kobayashi, K. Sueoka, *ECS J. Solid State Sci. Technol.* **2015**, *4*, P131.
- [56] D. A. Ramappa, W. B. Henley, *J. Electrochem. Soc.* **1999**, *146*, 3773.
- [57] J. Isenberg, S. Reber, J. Aschaber, W. Warta, in *European Photovoltaic Solar Energy Conference, International Conference*, Vol. 16, James & James, London **2000**, pp. 1463–1466.
- [58] J. Isenberg, S. Reber, W. Warta, *J. Electrochem. Soc.* **2003**, *150*, 365.
- [59] M. Takeda, T. Onishi, S. Nakakubo, S. Fujimoto, *Mater. Trans.* **2009**, *50*, 2242.
- [60] M. Baleva, V. Darakchieva, E. Goranova, E. P. Trifonova, *Mater. Sci. Eng., B* **2000**, *78*, 131.
- [61] C.-H. Hsu, D.-H. Huang, W.-Y. Ho, L.-T. Huang, C.-L. Chang, *Mater. Sci. Eng., A* **2006**, *429*, 212.
- [62] P. Hones, F. Lévy, N. Randall, *J. Mater. Res.* **1999**, *14*, 3623.
- [63] X. Pang, K. Gao, H. Yang, L. Qiao, Y. Wang, A. A. Volinsky, *Adv. Eng. Mater.* **2007**, *9*, 594.
- [64] E. J. Opila, N. S. Jacobson, D. L. Myers, E. H. Copland, *JOM* **2006**, *58*, 22.
- [65] G. Ziegler, H. J. Kleebe, G. Motz, H. Müller, S. Traßl, W. Weibelzahl, *Mater. Chem. Phys.* **1999**, *61*, 55.
- [66] R. D'Elia, G. Dusserre, S. Del Confetto, N. Eberling-Fux, C. Descamps, T. Cutard, *Polym. Eng. Sci.* **2018**, *58*, 859.